Newcastle University

ePrints

Woodward J, Taylor GC, Soares DC, Boyle S, Sie D, Read D, Chathoth K, Vukovic M, Tarrats N, Jamieson D, Campbell KJ, Blyth K, Acosta JC, Ylstra B, Arends MJ, Kranc KR, Jackson AP, Bickmore WA, Wood AJ.

Condensin II mutation causes T-cell lymphoma through tissue-specific genome instability.

***Genes & Development* 2016, 30, 2173-2186.**

Copyright:

This is the authors' accepted manuscript of an article that was published in its final definitive form by Cold Spring Harbour Laboratory Press, 2016.

DOI link to article:

http://dx.doi.org/10.1101/gad.284562.116

Date deposited:

02/12/2016

Embargo release date:

13 April 2017

This work is licensed under a Creative Commons Attribution-NonCommercial 3.0 Unported License

Newcastle University ePrints - eprint.ncl.ac.uk

Condensin II mutation causes T cell lymphoma through tissue-specific genome instability

Jessica Woodward[1], Gillian C Taylor[1], Dinesh C Soares[1,2], Shelagh Boyle[1], Daoud Sie[4], David Read[1], Keerthi Chathoth[1], Milica Vukovic[3], Nuria Tarrats[5], David Jamieson[6], Kirsteen J Campbell[7], Karen Blyth[7], Juan Carlos Acosta[5], Bauke Ylstra[4], Mark J Arends[5], Kamil R Kranc[3, 5], Andrew P Jackson[1], Wendy A Bickmore[1, 8], Andrew J Wood[1, 8]

[1]MRC Human Genetics Unit, Institute of Genetics and Molecular Medicine, University of Edinburgh, UK.

[2]Centre for Genomic and Experimental Medicine, Institute of Genetics and Molecular Medicine, University of Edinburgh, UK.

[3]MRC Centre for Regenerative Medicine, University of Edinburgh, UK.

[4]Department of Pathology, VU University Medical Center, The Netherlands

[5]Edinburgh Cancer Research UK Centre, Institute of Genetics and Molecular Medicine, University of Edinburgh, UK.

[6]Northern Institute for Cancer Research, University of Newcastle upon Tyne, UK.

[7]CRUK Beatson Institute, Switchback Road, Bearsden, Glasgow, G61 1BD.

[8] Correspondence to: Andrew.wood@igmm.ed.ac.uk

Wendy.bickmore@igmm.ed.ac.uk

Running title: Condensin II mutation promotes tumourigenesis in mice

Abstract

Chromosomal instability is a hallmark of cancer, but mitotic regulators are rarely mutated in tumours. Mutations in the condensin complexes, which restructure chromosomes to facilitate segregation during mitosis, are significantly enriched in cancer genomes, but experimental evidence implicating condensin dysfunction in tumourigenesis is lacking. We report that mice inheriting missense mutations in a condensin II subunit (*Caph2*^{nes}) develop T cell lymphoma. Before tumours develop, we find that the same *Caph2* mutation impairs ploidy maintenance to a different extent in different haematopoietic cell types, with ploidy most severely perturbed at the $CD4^+CD8^+$ T cell stage from which tumours initiate. Premalignant $CD4^+CD8^+$ T cells show persistent catenations during chromosome segregation, triggering DNA damage in diploid daughter cells and elevated ploidy. Genome sequencing revealed that *Caph2* single mutant tumours are near diploid but carry deletions spanning tumour suppressor genes, whereas *P53* inactivation allowed *Caph2* mutant cells with whole chromosome gains and structural rearrangements to form highly aggressive disease. Together, our data challenge the view that mitotic chromosome formation is an invariant process during development, and provide evidence that defective mitotic chromosome structure can promote tumourigenesis.

Introduction

Genome integrity is maintained by molecular machines that drive the duplication and segregation of the genome, and by checkpoints that monitor for incorrect execution of these processes. As cells enter mitosis, chromosomes undergo profound structural changes, which are driven by topoisomerase II and condensins (Swedlow and Hirano 2003). This process removes catenations between sister chromatids, generates stiff rod-like structures that are competent for chromosome segregation, and is essential for genome propagation through the cell cycle in all eukaryotes.

Condensins belong to the structural maintenance of chromosomes (SMC) complex family that also includes cohesin and SMC5/6. In eukaryotes, each SMC complex contains a heterodimer of SMC ATPase subunits, a single kleisin subunit and additional accessory factors (Nasmyth and Haering 2005; Losada and Hirano 2005) (Figure 1A). Within cohesin and condensin complexes, the carboxy and amino termini of kleisin interact with apposing SMC subunits to form a tripartite, asymmetric ring-like structure that can entrap DNA (Gruber et al. 2003; Onn et al. 2007; Cuylen et al. 2011; Piazza et al. 2014; Nasmyth and Oliveira 2010). This mode of association has been proposed to allow SMC complexes to form topological linkages between chromosomes, or between different regions on the same DNA molecule.

Metazoan genomes encode at least two distinct condensin complexes (Ono et al. 2003), which play non-redundant and incompletely understood roles in the regulation of chromosome architecture (Ono et al. 2003; Green et al. 2012; Hirano 2012; Houlard et al. 2015; Nishide and Hirano 2014).

Condensin I gains access to chromosomes between prometaphase and telophase, whereas condensin II is present in both the nucleus and cytoplasm during interphase and becomes concentrated on chromosome axes and centromeres during prophase (Hirota et al. 2004; Ono et al. 2004). Loss of condensin I results in shorter wider mitotic chromosomes, whereas loss of condensin II produces long chromosomes with reduced axial rigidity (Ono et al. 2003; Shintomi and Hirano 2011; Green et al. 2012).

Chromosome structure and mitotic fidelity are compromised in many cancers, which leads to numerical and structural chromosome abnormalities and DNA damage. The underlying causes of abnormal mitosis in cancer are not well understood, and it is notable that mutations in known mitotic regulators do not occur at high frequency in cancer genomes. However, successful mitosis requires the concerted activity of hundreds of genes (Neumann et al. 2010). Biologically significant mutations could therefore be distributed across a large number of loci at relatively low frequency per gene. Evidence supporting this hypothesis recently arose from a gene-network-based analysis of The Cancer Genome Atlas (TCGA) dataset (Leiserson et al. 2014). With the exception of SMC4, mutations in condensin subunits were not statistically enriched in tumour genomes when considered individually; however, statistical significance was reached when subunits were considered together as a single functional entity, reflecting their concerted activity in the cell.

Previous mouse models of condensin deficiency have focused primarily on loss of function mutations (Smith et al. 2004; Nishide and Hirano 2014;

Houlard et al. 2015), which cause chromosome segregation failure followed by cellular and organismal lethality. However, the majority of condensin mutations in TCGA are missense, and likely to exert sub-lethal effects on chromosome structure. To directly assess the consequences of hypomorphic condensin II deficiency on development and disease, we have studied a viable mouse model carrying a constitutive missense mutation in the condensin II kleisin-β subunit *Caph2* (*Caph2*^{nes}). These mice were previously reported to exhibit a block during T cell development resulting in thymic hypoplasia and reduced numbers of circulating T cells (Gosling et al. 2007). During T cell differentiation in wildtype mice, the earliest thymic progenitors do not express T cell receptor (TCR) and are double negative (DN) for CD4 and CD8. Successful VDJ recombination at the TCRβ-chain locus leads to progression through the β-selection checkpoint and rapid proliferation, during which cells upregulate CD4 and CD8 to become double positive (DP). These rapidly proliferating early DP cells express the transferrin receptor CD71 (DP CD71^{+}), but this marker is downregulated upon cell cycle exit (DP CD71^{-}) (Brekelmans et al. 1994), when rearrangement of the TCRα chain locus is completed. In *Caph2*$^{nes/nes}$ mice, T cell development is blocked at the transition from DN to DP (Gosling et al. 2007), but the cellular defects and their consequences during aging have not been characterised. We find that *Caph2*$^{nes/nes}$ mice develop thymic lymphomas with high penetrance, then identify the cell of origin and characterise the cytological and genomic abnormalities that drive condensin II-dependent tumour formation. Our data

provide direct experimental evidence that perturbation of the mitotic chromosome condensation apparatus can promote tumourigenesis.

Results

Caph2 mutation causes thymic lymphoma

The *Caph2*^{nes} allele (I15N) replaces an evolutionarily conserved hydrophobic amino acid for a polar residue in the N-terminus of Caph2 (Figure S1A). Based on available crystal structures (Bürmann et al. 2013; Kamada et al. 2013), the equivalent residue (I22) in prokaryotic condensins is largely buried and positioned within the first α-helix of the kleisin subunit (ScpA - Figure 1A & B). As reported previously (Gosling et al. 2007), the thymus and spleen of young *Caph2*$^{nes/nes}$ adults showed a marked reduction in T lymphocytes. Although *Caph2*$^{nes/nes}$ mice had lower body weight and reduced brain size compared to littermate controls (Martin *et al,* accepted at Genes & Development), the development of lymphoid organs was disproportionately affected (Figure S1B).

To determine whether sub-lethal condensin II perturbation predisposes to cancer, a cohort of *Caph2*$^{nes/nes}$ mice was aged for 15 months. Necropsy revealed lymphoma in 9 of 9 aged individuals compared to 0 of 8 controls (Fisher's exact $p < 1 \times 10^{-4}$, Figure 1C). Other than a single case of leiomyosarcoma in a *Caph2*$^{nes/nes}$ animal with concurrent lymphoma, no other tumours were identified upon necropsy. More than half of the *Caph2*$^{nes/nes}$ cohort became terminally ill within the 15 month study period (Log rank $p < 0.02$, Figure 1C). Lymphoma cells typically took over the thymus, spleen and

lymph nodes, and infiltrated lungs, kidneys and liver (Figure S1B and data not shown). Lymphoma cells were either $CD4^{+}CD8^{+}$ double positive (DP) or $CD4^{lo}CD8^{+}$ (Figure 1D), revealing their origin from thymic T progenitor cells that had progressed through the TCRβ-selection checkpoint.

The cell cycles following thymic β-selection are known to be particularly vulnerable to genomic instability, because the most rapid spontaneous tumours to develop in *P53* null mice are lymphomas with a $CD4^{+}CD8^{+}$ and immature $CD4^{lo}CD8^{+}$ immunophenotype (Donehower et al. 1992; Jacks et al. 1994). To assess the role of P53 during *Caph2*-dependent lymphomagenesis, $Caph2^{nes/nes}; P53^{-/-}$ double homozygous mutants (hereafter "double mutants") were derived by intercrossing $Caph2^{nes/nes}$; $P53^{+/-}$ parents. Double mutants were recovered at approximately Mendelian ratios (19% at weaning, $n = 121$, Fisher's exact $p = 0.35$).

To monitor the early stages of tumour development, we made use of the fact that each T cell undergoing β-selection carries a unique rearrangement at the T Cell Receptor β (TCRβ) locus. This can be used as a molecular barcode to quantify clonal expansion, where the proportion of identical V-D-J sequences detectable in genomic DNA from the thymus should increase (Supplemental Methods) (Dudgeon et al. 2014). Such increases can be detected by deep sequencing of PCR amplicons spanning the variable to constant regions of the TCRβ locus (Dudgeon et al. 2014). At three weeks *post partum* (*pp*), the highest proportion of replicated T cell clones in the thymus of *wildtype*, $Caph2^{nes/nes}$, or $P53^{-/-}$ single mutant animals ranged from 0.05% to 0.19%, indicating that no substantial clonal expansion

had occurred by this stage (Figure 2). In contrast, the thymus of double mutant animals already contained several expanded clones by three weeks *pp*, with 4 or 5 distinct clones each comprising >1% of total sequence reads, and at least one clone accounting for >20% of TCRβ rearrangements detected (Figure 2). Clonal expansion in *P53*$^{-/-}$ single mutant animals is first detectable at nine weeks *pp* (Dudgeon et al. 2014); hence, *Caph2* mutation greatly accelerates the outgrowth of clonal T cell populations in the thymus of juvenile *P53*$^{-/-}$ animals.

An aging cohort of 14 double mutants all became terminally ill within 100 days (median survival = 81 days, Figure 1C), with massive thymic lymphoma apparent in every case. This represents a substantially reduced survival relative to either mutation alone (median 447 days for *Caph2*$^{nes/nes}$, 144 days for *P53*$^{-/-}$ (Figure 1C), Log-rank $p < 0.001$ for both comparisons). No evidence of non-lymphoid tumours was observed upon necropsy of double mutant animals.

Abnormal metaphase chromosome structure and anaphase in *Caph2*$^{nes/nes}$ thymocytes

It has previously been reported that thymic T cell development is impaired during the DN to DP transition in young adult *Caph2*$^{nes/nes}$ individuals (Gosling et al. 2007), which is also the stage during which our data reveal that lymphomas arise in aged animals (Figure 1D). The cellular defects that block T cell development in *Caph2*$^{nes/nes}$ animals are known to be T cell autonomous and independent of VDJ recombination (Gosling et al. 2007), but it is not

known whether they affect mitosis, or possible alternative functions of condensin II during interphase (Gosling et al. 2007; Rawlings et al. 2010; Wood et al. 2010).

Although we found that interphase cells at the DP stage were increased in size in *Caph2*$^{nes/nes}$ animals, this was attributable to increased ploidy, rather than interphase chromosome decompaction, because no difference in size was apparent between wildtype and mutant cells of equivalent DNA content (Figure S2A). No evidence for localised chromatin decondensation was observed in analyses of mean squared distances (d^2) between FISH probes (Eskeland et al. 2010) separated by 0.1Mb at the non-expressed *HoxA* locus (Figure S2B), or by 0.1Mb, 1Mb and 5Mb at the expressed *CD8* locus (Figure S2C) in DP CD71$^+$ *Caph2*$^{nes/nes}$ cells. Radial positioning (Figure S2D), and chromocenter clustering (JW, unpublished data) were also not significantly affected by *Caph2* mutation.

Expression microarray comparisons between DP thymocyte subsets from *Caph2*$^{+/+}$ and *Caph2*$^{nes/nes}$ animals revealed only subtle effects on the transcriptome (R^2 = 0.99), as expected for comparisons between carefully stage-matched cell populations (Figure S3A). However, gene ontology enrichment analysis performed on gene lists ranked by fold change revealed functional classifiers that were strongly enriched among genes upregulated in *Caph2*$^{nes/nes}$ cells (Figure S3). In both the rapidly cycling CD71$^+$ and the quiescent CD71$^-$ DP population, the most significantly enriched terms centred on metabolism and proteostasis (Figure S3B, Figure S3C, Table S1 & S2). Each of these processes has recently been implicated in the cellular stress

response to aneuploidy (Williams et al. 2008; Torres et al. 2007; Sheltzer et al. 2012). Thus, although a tumour-causing mutation in *Caph2* influences the size and transcriptional profile of pre-malignant cells, both differences are consistent with perturbation of the mitotic cell cycle. However, more subtle direct effects on interphase chromosome structure cannot be excluded.

We next sought evidence of abnormal cell cycle progression in premalignant *Caph2*$^{nes/nes}$ cells from the relevant developmental stage. DN thymocytes were purified from young adults, before tumour onset, by fluorescence activated cell sorting (FACS) and cultured on monolayers of OP9-DL1 stromal cells (de Pooter and Zúñiga-Pflücker 2007), where they undergo extensive proliferation and differentiate into DP cells. *Caph2*$^{nes/nes}$ thymocytes showed impaired proliferation and differentiation in this *ex vivo* system (Figure S4A, S4B), validating its utility for mechanistic studies.

To address whether mitotic entry was delayed in primary *Caph2*$^{nes/nes}$ thymocytes, we used a BrdU chase assay to follow the kinetics of progression from S phase into M phase (Figure 3A). BrdU and nocodazole were added simultaneously to day 5 OP9/DL1 cultures, in order to label cells in S phase, and to arrest cells in prometaphase, respectively. Over a four hour time course, we then used flow cytometry to measure the fraction of BrdU labelled cells in mitosis, based on expression of the mitotic marker histone H3 phosphorylated at serine 10 (pH3S10). *Caph2* mutation did not affect the rate at which BrdU labelled cells accumulated in mitosis (two-tailed t-test $p > 0.1$ for all time points).

To determine whether cell cycle progression was impaired after mitotic entry, immunofluorescence was performed on thymocytes grown on OP9-DL1 co-cultures in the absence of nocodazole, using antibodies against alpha-tubulin and pH3S10, and the proportion of $pH3S10^{+}$ cells at different stages of mitosis was assessed. Cells at later stages (late anaphase & telophase) were significantly underrepresented relative to earlier stages in the *Caph2*$^{nes/nes}$ mutant cultures (Fisher's exact $p < 0.003$, Figure 3C), indicating a cell cycle block that impaired progression into successful anaphase. To enrich for anaphase cells, primary *Caph2*$^{nes/nes}$ thymocytes from OP9/DL1 co-cultures were released into anaphase following wash-out of the proteasome inhibitor MG132. Immunofluorescence revealed an elevated frequency of abnormalities (Fisher's exact $p < 0.0001$), primarily comprising anaphase bridges plus occasional lagging chromosomes, multipolar spindles and micronuclei (Figure 3D & 3E). These mitotic abnormalities are likely to originate from defective mitotic chromosome structure, because metaphase chromosomes showed a characteristic "zig-zag" appearance following hypotonic treatment (Figure 3F), similar to previous reports of condensin II deficiency in immortalised vertebrate cells (Ono et al. 2003; Green et al. 2012). Abnormal mitosis had a profound effect on the ploidy of proliferating DP thymocytes, with an accumulation of cells with a DNA content of 4N or greater (Figure S4C). Importantly, T cells with abnormal ploidy were already abundant in neonatal *Caph2*$^{nes/nes}$ mice (Figure S4C), substantially before clonal expansion is first detectable (Figure 2). The profound mitotic

abnormalities evident in *Caph2*$^{nes/nes}$ T cells therefore precede malignant transformation, and cannot be a downstream consequence.

Given that mitosis is thought to be a cell-type invariant process, we next sought to determine whether ploidy is perturbed to a similar extent in all cell types of *Caph2*$^{nes/nes}$ mice. Multiparametric flow cytometry was used to compare cellular DNA content as haematopoietic stem and early progenitor cells from *Caph2*$^{nes/nes}$ and control animals differentiate into αβ-T and B lymphocytes *in vivo* (Figure 4, Figure S5, Figure S6). This revealed that ploidy was largely unaffected by *Caph2* mutation in bone marrow progenitor populations, B cells and early thymic T cell subsets, with abnormalities becoming evident only from the β-selection stage of T cell development onwards (Figure 4, Figure S5). This cell-type-specific phenotype was not simply attributable to a greater proportion of proliferating cells, because BrdU incorporation was detected in a comparable percentage of DP CD71^{+} T cells (61% - Figure S5H) and B cells at the Fraction C stage (59% - Figure S5D) in wildtype mice, yet abnormal ploidy in *Caph2* mutants was restricted to T cells (Figure 4).

Together, these data demonstrate that germline hypomorphic mutation in *Caph2* impairs cell cycle progression at a specific stage of αβ-T cell development; CD4^{+}CD8^{+} thymocytes enter mitosis with normal kinetics but abnormal chromosome structure, which leads to anaphase bridges and impaired mitotic progression in pre-malignant cells, preceding tumour initiation. Moreover, our studies of haematopoietic differentiation demonstrate that the same mutation in condensin II can elicit different effects on

chromosome segregation in different proliferative cell types, which suggests that the formation of segregation-competent mitotic chromosomes is a developmentally regulated process.

Exit from Caph2 deficient mitosis leads to DNA damage, tetraploidy, and *P53* activation

Using imaging flow cytometry, we next assessed the incidence of DNA damage in primary thymocytes at different phases of the cell cycle by the simultaneous quantification of γH2AX foci, BrdU incorporation and DNA content (Figure 5A - C). In the smallest 25% of cells with 2N DNA content, which includes cells that have recently completed mitosis, γH2AX foci occurred in 85% of *Caph2*$^{nes/nes}$, compared to just 2% of *wildtype* cells (Figure S7). The average number of discrete γH2AX foci per nucleus was also significantly increased by *Caph2* mutation (Figure 5C, Figure S7B). However, elevated frequencies of cells with γH2AX foci were also observed in S and G2 phase (Figure 5B), which could be explained by defective DNA repair or the ongoing acquisition of damage during S phase.

In addition to diploid cells with DNA damage, we found an abundance of abnormally large DP cells that had undergone cell cycle arrest (Figure 6A and 6B). Quantification of DNA content in this population revealed that they were 4N (Figure 6C), suggesting arrest during either G2, or in a tetraploid G1 phase. However, given that *Caph2*$^{nes/nes}$ thymocytes progress from S phase to M phase with normal kinetics (Figure 3B), we hypothesised that a tetraploid G1 was the more likely scenario. To confirm this, we assessed sister

chromatid cohesion in FACS-purified 4N cells using fluorescence *in situ* hybridisation (FISH) experiments that combined fosmid probes and chromosome paints (Figure 6D). This revealed that, contrary to the expectation for a G2 cell, the four chromosomal homologs were typically not subject to sister chromatid cohesion (Figure 6D). We therefore conclude that these arrested 4N cells, which make up at least 20% of all $CD4^{+}CD8^{+}$ cells in the *Caph2*$^{nes/nes}$ thymus (Figure 6A & B), are arrested in a tetraploid cell cycle phase resembling G1, presumably following mitotic exit without completing chromosome segregation and cytokinesis.

P53-dependent checkpoints ordinarily limit the proliferation of cells with DNA damage (Kastan et al. 1991; Lowe et al. 1993) and abnormal ploidy (Fujiwara et al. 2005; Thompson and Compton 2010), and play a key role in suppressing lymphomagenesis in both wildtype (Donehower et al. 1992) and *Caph2*$^{nes/nes}$ animals (Figure 1C, Figure 2). To interrogate the signalling pathways operating downstream from P53 in *Caph2*$^{nes/nes}$ thymocytes, we assessed the expression of 84 known P53 targets by qRT-PCR in non-cycling ($CD71^{-}$) DP cell populations isolated from young animals, prior to tumour establishment. Key regulators of apoptosis (*Noxa*, *Fas*) and cell cycle arrest (*Cdkn1a*) were upregulated by >2.5-fold in *Caph2*$^{nes/nes}$ thymocytes in a P53-dependent manner (Figure S8A, Table S3). Notably, we found that the upregulation of P53 targets occurred in cells with 2N, as well as 4N DNA content (Figure S8B), demonstrating that P53 signalling is activated regardless of whether cells exit mitosis in a diploid or tetraploid state.

_P53_ status determines copy number changes in _Caph2_ mutant tumours

To characterise genomic changes which accompany lymphomagenesis in *Caph2* mutant T cells, we performed shallow whole genome sequencing (Scheinin et al. 2014) of genomic DNA extracted from terminal tumours of animals with germline mutation in *Caph2* and *P53* (Figure 7, Figure S9). Whole chromosome aneuploidy (WCA) was rare in terminal tumours from *Caph2*$^{nes/nes}$ single mutants (*n* = 7 tumours, mean WCA = 1.4, median WCA = 1)(Figure 7B). Absolute copy number enumeration of selected loci by FISH (Figure S10) confirmed that *Caph2*$^{nes/nes}$ single mutant tumours were near diploid rather than tetraploid. Although deletions spanning the *P53* locus were not apparent in *Caph2*$^{nes/nes}$ single mutant lymphomas, several top scoring deletions encompassed key P53 pathway components such as *Cdkn2a* and *Pten*, and other known suppressors of human T cell malignancy such as *Bcl11b* (Gutierrez et al. 2011) (Table S4). Thus, despite the abundance of tetraploid cells in the premalignant DP population (Figure 4, Figure 6, Figure S4C), these data argue that tumours from *Caph2*$^{nes/nes}$*; P53*$^{+/+}$ mice initiate from cells that acquire DNA damage and mutation without undergoing genome doubling (Figure 5, Figure S7).

Tumours from double mutant animals contained significantly more whole chromosome aneuploidies than *Caph2*$^{nes/nes}$ single mutants (*n* = 13 tumours, mean WCA = 7.3, median WCA = 6, two-tailed t-test $p < 0.001$) (Figure 7B & Figure S9). Double mutant tumours also contained, on average, two to three-fold more segmental copy number aberrations (CNAs) compared to *Caph2* single mutant tumours, and over twenty-five-fold more than tail DNA

(Figure 7C & D). Recurrently amplified regions contained known oncogenic drivers of human T cell lymphoma, including *Notch* (12 of 13 tumours) and *Ptpn14* (11 of 13 tumours). We conclude that the large population of cells with abnormal ploidy, that is present in the *Caph2*$^{nes/nes}$ thymus before clonal expansion, has the potential to form highly aggressive tumours but is ordinarily prevented from doing so by a P53-dependent mechanism.

Discussion

In this report we provide experimental support for the hypothesis that condensin dysfunction can promote tumourigenesis (Hirano 2012; Longworth et al. 2008; Manning et al. 2010; Coschi et al. 2010; 2014; Ham et al. 2007). We found that tumours initiate from thymic T cells progressing from the DN to DP stage, which allowed us to characterise the cellular abnormalities that precede, and therefore presumably drive, *Caph2*-dependent malignancy. Through detailed cytological analysis of tumour initiating cells in the thymus of *Caph2*$^{nes/nes}$ mice, we show that a tumour-causing mutation in *Caph2* does not promote global decondensation of interphase chromatin (Figure S2), or major changes in developmental gene expression programs (Figure S3). However, we leave open the possibility that the *Caph2*^{nes} mutation impairs interphase processes in a manner that was not detected in our study.

Abundant evidence was obtained for a direct effect of the *Caph2*^{nes} mutation on mitosis. Tumour-initiating cells at the DP 71^{+} stage of T cell differentiation show impaired mitotic progression, but not mitotic entry (Figure 3), and generate two distinctly abnormal cell populations upon mitotic exit. Diploid cells show extensive DNA damage (Figure 5, Figure S7), and we propose that when such damage yields mutations in tumour suppressor genes such as *Cdkn2a*, *Pten* or *Bcl11b* (Table S4), this population can give rise to the near diploid lymphomas observed in aging *Caph2*$^{nes/nes}$ animals (Figure 7A, Figure S9, Figure S10). In addition, a large fraction (>20%) of all DP thymocytes in young *Caph2* mutants exit mitosis in a tetraploid state (Figure 6B & 6C).

The fact that tumours in *Caph2*$^{nes/nes}$ animals with an intact P53 pathway do not show frequent whole chromosome gains argues that tetraploidy does not promote malignancy in the presence of P53, consistent with previous reports (Fujiwara et al. 2005). Under these circumstances, we speculate that mitotic exit in the tetraploid state may be a more favourable outcome for cells with persistent catenations than completion of chromosome segregation with DNA damage, because the latter has greater potential to generate oncogenic mutations.

Disease progression is markedly accelerated when the P53 pathway is disabled (Figure 1C), where abnormal clonal outgrowth is readily detectable by deep sequencing of the TCRβ repertoire during the first three weeks of life (Figure 2). In a *Caph2*$^{nes/nes}$ *P53*$^{-/-}$ background, dominant clones exhibit multiple whole chromosome gains (Figure 7A, Figure S9D) or evidence of genome doubling (Figure S9D). The high fraction of viable tetraploid cells that arise spontaneously in the *Caph2*$^{nes/nes}$ thymus (Figure 6), combined with the rapid and highly reproducible course of disease progression in *Caph2*$^{nes/nes}$ *P53*$^{-/-}$ animals (Figure 1C, Figure 2), provides an attractive model for future studies on the pathological consequences of genome doubling *in vivo*.

In a companion paper we describe a cohort of four human patients with germline condensin mutations that result in microcephalic primordial dwarfism (Martin *et al*, accepted at *Genes & Development*). One of these patients died from malignant anaplastic medulloblastoma at the age of 11, which suggests that germline condensin deficiency may increase the risk of tumourigenesis in humans. Somatic condensin mutations occur in a small but statistically

significant fraction of human cancers (4.2% (Leiserson et al. 2014)), and a large majority of condensin mutations in the COSMIC database (http://cancer.sanger.ac.uk/cosmic) are missense substitutions analogous to *Caph2*^{nes} (Figure 1B, Figure S1A). However, genomic analyses of human T cell leukemias and lymphomas (Zhang et al. 2012; Kataoka et al. 2015) indicate that condensin mutations are no more frequent than in other tumour types, suggesting that the strong tissue-selectivity reported here is likely to be species-specific. The reasons that murine T cell development is uniquely vulnerable to global condensin II mutation are likely to be multifaceted, but could involve kinetic properties of the cell cycle, or stress responses arising from aberrant mitosis that distinguish the highly proliferative cells at the DN to DP transition from other somatic cell types.

Several recent reports have provided evidence that condensin II function could be impaired in human tumours via a more widespread mechanism that does not require mutations in the core complex (Longworth et al. 2008; Manning et al. 2010; Coschi et al. 2010; 2014). Mutations in the *Rb* tumour suppressor, which is among the most frequently mutated genes in a broad range of human tumours, partially impair condensin II loading and function (Longworth et al. 2008; Manning et al. 2010; Coschi et al. 2010; 2014). This provides a possible explanation for the high levels of chromosomal instability reported in Rb1-deficient tumours, and, together with the data reported here, suggests that the clinical relevance of this alternative Rb1 function should be carefully evaluated.

Materials & Methods

Animals and primary cell isolation

The animal studies described in this paper were carried out under the guidance issued by the Medical Research Council in Responsibility in the Use of Animals for Medical Research (July 1993) and Home Office Project Licence no PPL60/4424. Animals were housed in individually ventilated cages within the Biomedical Research Facility at the Western General Hospital, Edinburgh. Tumour samples from $P53^{-/-}$ tumours used for copy number analysis were from animals housed in the BSU facilities at the CRUK Beatson Institute under project license PPL60/4181. The *Caph2*^{nes} (Gosling et al. 2007; Nelms and Goodnow 2001) and *P53*$^{-}$ (Jacks et al. 1994) mutations were generated as described previously, and maintained on a C57BL6/J background. Unless otherwise stated, non-tumour tissues were harvested from 6 – 12 week animals and processed immediately. No differences in T cell phenotype were observed between male and female mice; hence, animals of either gender were used interchangeably. Female mice were used for all aging studies, with the exception of the *Caph2*$^{nes/nes}$ *P53*$^{-/-}$ genotype, for which males were used due to a low frequency of female mice recovered.

Single cell suspensions were obtained from thymus by gentle tissue dissociation through a 40 micron filter, and from femur and tibia by flushing bone cavities with PBS (B cells), or by crushing bones with a pestle and mortar (LSK and CLP populations). Tissues were collected and processed immediately following termination, and cell counts were conducted on a moxi-

Z automated cell counter (ORFLO). For BrdU incorporation studies 150 µl of 10mg/ml BrdU solution was injected into the intraperitoneal cavity two hours prior to termination.

Cell culture

For primary T cell cultures, $CD4^+$ and $CD8^+$ thymocytes were depleted using MACS beads (Miltenyi) according to manufacturer's instructions. For the proliferation and differentiation assays shown in Figure S4 and the mitotic studies shown in Figure 3, DN3 cells were then purified by FACS using surface expression of CD25 and CD44. For the BrdU chase experiment in Figure 3A & B, total DN cells were seeded, whereas for all other OP9/DL1 experiments of mitosis and cell cycle progression, DN3 cells were seeded directly following FACS purification. Details of cell surface marker combinations used for immunophenotyping are listed in Table S5. 1 – 5 x 10^5 total DN cells or 2.5 x 10^4 DN3 cells were seeded onto each well of a 6 well plate, containing subconfluent monolayers of OP9-DL1 stromal cells in α-MEM medium (+nucleosides) supplemented with 20% Fetal Bovine Serum, 1% Pen/Strep, 15µM β-Mercaptoethanol and 1ng/ml IL-7 (Peprotech). Cell cycle studies were conducted 4 or 5 days after seeding total DN cells, when lymphocytes were removed from monolayers by gentle pipetting, then passed through a 40uM filter to remove clumps of stromal cells before further processing. For BrdU chase experiments, BrdU (10µM final concentration) and nocodazole (300ng/ml) were added to cultures on day 4 or 5, then cells were collected at the specified time points before staining for cell surface

markers, pH3S10 and BrdU using the APC BrdU Flow kit (BD Pharmingen), according to manufacturers instructions, with pH3S10 antibody added at the same time as anti-BrdU.

Immunofluorescence

Cells from OP9-DL1 co-cultures were washed once with PBS and allowed to settle on poly-lysine-coated coverslips before. For MG132 release, MG132 (Cayman) was added to day 4 OP9/DL1 co-cultures to a final concentration of 15µM. After two hours, T cells were removed by gentle pipetting, washed once with PBS and seeded on fresh OP9-DL1 monolayers in media lacking MG132. After 60 minutes, T cells were removed by gentle pipetting and allowed to settle on poly-lysine-coated coverslips. Cells were fixed in 4% paraformaldehyde for 10 mins, washed 3 x 5 minutes in PBS (hereafter "washed"), permeabilised in 0.5% TritonX in PBS for 10 minutes, washed, blocked in goat or donkey serum (5% in PBS) for 30 minutes, incubated with primary antibodies at 4°C overnight, washed, incubated with secondary antibodies for 1 hour at room temperature, washed, incubated in 0.5µg/ml DAPI for 5 minutes and then mounted in vectashield (vector labs). Antibodies used in this study are listed in Table S6.

Metaphase spreads

To generate metaphase spreads, cells were treated with hypotonic solution (0.5% sodium citrate, 0.25% potassium chloride in deionised water) and fixed in 3:1 methanol: acetic acid, added drop-wise whilst vortexing the sample.

The samples were incubated at room temperature for 30 minutes, before centrifugation, re-suspension in 10mL fix, and overnight storage at -20^{o}C. The cell suspension was dropped on to high precision cover-glass (Marienfelt, Germany), stained with DAPI (50ng/ml in PBS) and mounted in Prolong Gold (Life Technologies). 3D SIM images were acquired on a N-SIM (Nikon Instruments, UK) using a 100x 1.49NA lens and refractive index matched immersion oil (Nikon Instruments). SIM images were reconstructed using NiS Elements software (Nikon Instruments) from a z stack comprised of no less than 1um of optical sections.

FISH probe synthesis, hybridisation and image analysis

To prepare nuclei for three dimensional FISH, cells were allowed to settle on poly-lysine-coated slides then fixed in 4% PFA for 10 minutes at 37°C, washed, permeablised in 0.5% Triton X in PBS for 10 minutes, washed, and then left to dehydrate at room temperature, before being stored at -80oC for up to 2 months. Upon thawing, slides were rinsed in 2xSSC then incubated in 2xSSC containing 100 µg /mL RNase (Roche) at 37°C for 1 hour. Slides were washed in 2xSSC and then dehydrated through a series of two minute ethanol washes (70%, (90% and 100%) before being air dried. Slides were then heated in a 70°C oven for five minutes and denatured for 30 minutes at 80°C in 70% formamide/2xSSC, pH7.5. The slides were transferred to ice-cold 70% EtOH for two minutes, before further dehydration in 90% and 100% ethanol at room temperature, for two minutes each.

With the exception of the experiment presented in Figure 5 (see below), all FISH probes were generated from fosmids (details in Table S7). To prepare fosmid probes, DNA was isolated using standard alkaline lysis and labelled by nick-translation with digoxigenin-11-dUTP or biotin-16-dUTP (Roche). Approximately 70 - 100ng of fosmid was used per slide, together with 18ug mouse Cot1 (Invitrogen) DNA and 5ug of salmon sperm DNA (Sigma). Ethanol precipitated DNA was resuspended in 15uL hybridisation mix (50% deionised formamide, 10% dextran sulphate and 1% Tween 200 in 2xSSC). Probes were denatured at 70°C for five minutes and then reannealed at 37°C before being applied to the slide and sealed under a coverslip at 37°C. After 48 hours, coverslips were removed and slides underwent 4 x 2 minute washes in 2X SSC at 45°C, then 4 x 3 minute washes in 0.1X SSC at 60°C. Slides were then transferred to 4X SSC/0.1% Tween at room temperature before a 5 minute incubation with blocking buffer (4X SSC, 5% Marvel) under a coverslip. Biotinylated probes were detected using Texas Red (TR)-conjugated avidin (1mg/mL stock diluted 1:500 in blocking buffer), followed by biotinylated antiavidin (BAA) (0.5mg/µL diluted 1:100) and a final layer of TR-conjugated avidin (1mg/mL diluted 1:500). Digoxigenin-labeled probes were detected with sequential layers of Fluorsecein isothiocyanate (FITC)-conjugated antidigoxigenin (200µg/mL diluted 1:20) and FITC-conjugated anti–sheep (1.5mg/mL diluted 1:100). All antibodies were obtained from Vector Laboratories with the exception of FITC-conjugated anti-digoxigenin which was obtained from Roche. Antibody incubations were carried out in a humid chamber at 37°C for 30-60 minutes, followed by 3 x 2 minute washes in

4xSSC/0.1% Tween at 37°C before the addition of the next layer of antibody. After the last antibody incubation, slides were incubated in 4X SSC/0.1% Tween with 50ng/mL DAPI for 2 minutes before mounting in Vectashield (Vector labs).

For the experiment to assess sister chromatid cohesion presented in Figure 5D & 5E, both the chromosome 2 exome paint and 130kb HoxD-specific probe were generated by direct labelling of liquid-phase oligonucleotide pools obtained using sequence capture technology (Boyle et al. 2011). The oligonucleotide isolation, labelling and hybridisation steps were performed as described previously (Boyle et al. 2011). To assess sister chromatid cohesion, we FACS purified 4N cells and counted the number of distinct HoxD signals per nucleus. For quantification purposes, only signals separated by >0.5μM were counted. Probes generated from oligonucleotide pools (Figure 5D & 5E) lack repetitive sequences, and hence false positive signals are greatly reduced.

Flow Cytometry, FACS and Imaging Flow Cytometry

Single cell suspensions were incubated with antibodies against cell surface antigens at room temperature for 10 minutes and washed once in PBS prior to analysis. The combination of cell surface markers used to identify each cell population is listed in Table S5, with antibody details in Table S6. For DNA content analysis, surface stains were fixed using the CytoFix/CytoPerm kit (BD) according to manufacturers instructions, before a secondary fixation step in cold 70% ethanol for 20 minutes at 4°C, wash in cytoperm buffer (BD

Pharmingen) before resuspension in cytoperm buffer containing 10µg/ml DAPI. Data were acquired on a BD FACSAria II cell sorter or BD LSRFortessa cell analyser, and processed using FlowJo software (Treestar). DNA content measurements by flow cytometry are susceptible to artifacts arising from cell aggregates. For all conventional flow cytometry experiments, we performed strict aggregate exclusion based on area versus height of the DAPI and Forward Scatter signals (data not shown). We also validated our finding of elevated polyploidy in *Caph2*$^{nes/nes}$ cells using imaging flow cytometry and FISH (data not shown).

BrdU staining was performed using the APC BrdU Flow kit (BD Pharmingen) according to manufacturer's instructions. For quantification of γH2AX positive cells at different cell cycle stages, total thymocytes were isolated from the thymus of mice two hours following BrdU injection, and stained with anti-BrdU-APC, anti-γH2Ax-FITC and DAPI, using the BrdU Flow kit protocol (BD Pharmingen). Fluorescent and brightfield images were captured using an ISx MKII (Amnis) using a 60X objective. Following acquisition and compensation the data was analysed with IDEAS (Amnis) software, using a modified version of published methods (Parris et al. 2015) as follows. In addition to the automatically generated system image masks three further masks were built. The first mask eroded the DAPI mask by two pixels to ensure any perinuclear signal was not included in subsequent analysis of nuclear staining patterns and intensities. A second mask was generated based on FITC intensity, removing pixels with an intensity of 600 or less, to remove background and nonspecific staining, and to ensure only

clearly defined intense spots were retained for counting. A third mask used a Boolean instruction to combine the two masks described above to ensure that only FITC foci localised to the region of the nuclei were counted. A spot count feature was generated based on the combined mask.

A data analysis pathway identified round single cells (RSCs) on the basis of size and circularity of the bright field images. Gated RSCs were input into a histogram to select cells in focus, based on the intensity of adjacent pixels in an image (the Gradient Root Mean Squared function). In focus round single cells were then used as the population in a histogram to identify BrdU positive and negative cells. 2N, and ≥4N cells were identified from the BrdU negative population based on DAPI fluorescence. The three populations were plotted by number of γH2AX foci against overall γH2AX staining intensity (e) and cells with at least one focus above an intensity threshold categorised as γH2AX positive.

T Cell Receptor Sequencing

DNA was extracted from flash frozen thymus tissue using DNeasy blood and tissue kit (Qiagen). The TCRβ locus was sequenced using the ImmunoSeq Assay (Adaptive Biotechnologies) at survey level resolution, using 0.8 – 1µg of starting material. PCR amplicons spanning the variable to constant sections of the TCRβ chain were sequenced using the illumina MiSeq platform, and potential PCR biases were controlled using algorithms provided by Adaptive Biotechnologies (Carlson et al. 2013). Data were analysed using the ImmunoSeq data analysis portal on the Adaptive Biotechnologies website.

The two samples from $P53^{-/-}$ single mutants were from a published study (Dudgeon et al. 2014), for which the data were available through the Immunoseq portal for analysis alongside the data generated for this study.

Copy Number Data Generation

Genomic DNA was isolated from FFPE tumour samples using the BioStic FFPE kit from Mo Bio laboratories, and from flash frozen tumour samples using the DNAeasy kit from Qiagen. Copy number analysis was performed as previously described (Scheinin et al. 2014). In brief, DNA was sheared with a Covaris S2 (Covaris) followed by the TruSeq NANO kit V2 (Illumina). Final sequence library amplification was performed with 10 PCR cycles for the FFPE-derived DNA samples and 8 PCR cycles for DNA derived from fresh samples. The yield of the sequence library was assessed with a DNA 7500 chip on a 2100 BioAnalyzer (Agilent Technologies). A double-sided bead size selection procedure with Agencourt AMPure XP beads (Beckman Coultier) was performed to clean the DNA preparations. The barcoded mouse samples were equimolarly pooled, and 12.5 pM molarity with 1% phiX was loaded on a HiSeq Single End Flowcell (Illumina). This was followed by cluster generation on a cBot (Illumina) and sequencing on a HiSeq 2500 (Illumina) in a single-read 50-cycle run mode (SR50-HTV4). BAM files have been submitted to the Sequence Read Archive (NCBI) under experiment ID SRX1391296. (final accession pending curation of data)

Copy Number Data Analysis

The mouse reference version GRCm38/mm10 was used to determine GC content and mappability. GC content was calculated for 30kpb and 1Mb bin sizes and mappability was determined with GEM-mappability (Derrien et al. 2012) allowing two mismatches. Loess residuals, used to make a mouse C57BL/6J specific blacklist, were calculated with 24 samples obtained from a publicly available normal mouse C57BL/6J data set (Gnerre et al. 2011). Only the first 50bp of the forward read were included for residual calculation. In addition, the 50bp reads of the 3 normal mouse C57BL/6J samples, sequenced in parallel with the tumors, were included in the residual calculations. The data was analysed with QDNAseq version 1.4.2 (Scheinin et al. 2014). Copy number profiles were segmented with DNAcopy (Venkatraman and Olshen 2007) and copy number aberrations were called by selecting segments with a log2-ratio higher than 0.20 or lower than -0.23, corresponding to a single gain or a single loss in 30% of the analysed cells (van Thuijl et al. 2014). Breakpoints were defined at the junction between bins of different copy number according to the criteria above. For the deletion list in Table S4, we started with all regions of copy number loss in *Caph2*$^{nes/nes}$ single mutant tumour samples, and removed regions corresponding to the X chromosome and T Cell Receptor loci, in addition to regions also deleted in *Caph2*$^{nes/nes}$ tail DNA. The remaining regions were ranked according to $\log_2$ ratio, and the top ten ranking regions were manually curated to identify tumour suppressor genes.

Homology detection and structural interpretation of mutation

The mouse Caph2 sequence was used to search for homologous structures using the HHPred server(Söding et al. 2005). Three bacterial condensin structure hits (PDB IDs: 4I98_A; 3ZGX_C; 3W6J_A) were returned with their corresponding alignment that includes the first two alpha-helices. Additional Caph2 vertebrate orthologues were detected with a BLAST search against the SwissProt database at the NPS@ server(Combet 2000), and included into the multiple sequence alignment with minor manual editing. Figure 1B was prepared using ESPript version 3(Gouet et al. 2003). Intra-protein interactions for the I15N equivalent residue in *B.subtilis* (I22) were analysed using the Protein Interactions Calculator (PIC)(Tina et al. 2007) using a 5 Å sphere radius cut-off. Residue-specific solvent accessibility calculations were performed using ASAView(Ahmad et al. 2004). Structure visualisation and analysis, and the preparation of Figure 1B, was conducted using PyMOL (http://www.pymol.org/; Schrödinger LLC, USA).

Transcriptome Analysis

Total RNA was extracted using TRIzol reagent (Life technologies), and RNA quality was assessed using Bioanalyzer (Agilent). From each of three biological replicates per sample (cell purification scheme detailed in Figure S3A), 80ng RNA was amplified and biotinylated using the MessageAmp II kit (Ambion). 750ng cRNA was hybridised to Mouse Ref-8 v2 Expression Beadchips (Illumina) using Whole-Genome Expression Direct Hybridisation kit (Illumina) and scanned with a Highscan (Illumina). Raw data were analysed using Bioconductor within the FlexArray software package

(http://genomequebec.mcgill.ca/FlexArray). RMA background adjustment, variance stabilisation transformation (VST) and robust spline normalisation were applied. Mean signal values were calculated at the gene level using ANOVA, and tests for difference between sample types were conducted using equal variance t-tests. Using conventional cutoffs for statistical significance (>2-fold change, $p < 0.05$), very few transcripts were returned as differentially expressed between stage-matched DP thymocyte populations. To identify more subtle trends, all genes on the array with associated Ensembl and gene symbol annotations were first ranked according to fold change (*Caph2*$^{nes/nes}$ / *Caph2*$^{+/+}$), and the ranked list was used as the input for gene ontology term enrichment within the "Process" classification using the GOrilla tool (2009). Full lists of terms returned by the GOrilla tool are listed in Tables S1, S2 and S8. MIAME-compliant microarray data are available under GEO accession GSE65199.

qRT-PCR

For the qPCR array experiments depicted in Figure S8A and Table S3, DP CD71$^-$ cells were purified from thymocytes that were first enriched for CD4$^+$ cells by MACS (miltenyi), then FACS purified for CD4$^+$, CD8$^+$ and CD71$^+$ using the scheme outlined in Figure S4C. Cell purity was typically 85 – 95%. Total RNA was extracted from cells using TRIzol reagent (Life technologies), followed by purification through an RNAeasy colum (Qiagen). RNA quality was assessed using Bioanalyzer (Agilent). From each of two biological replicates per sample, 100ng RNA was reverse transcribed using the RT^2

first-strand kit (Qiagen). qRT-PCR was performed on technical #quadruplicates using the mouse P53 pathway qRT-PCR array (Qiagen: PAMM-027Z). Normalisation and all downstream analysis steps were performed according to the manufacturer's instructions, and data analysis was conducted using the RT^2 profiler PCR-array software (Qiagen). For the experiment in Figure S6B, total thymocytes were incubated with Hoechst for 30 minutes in Hanks balanced salts solution, then sorted according to DNA content and processed as above using primers designed in house. All qRT-PCR data in Figure S6A, S6B and Table S3 represent mean values from two biological replicate experiments, each comprising two technical replicate PCRs.

Acknowledgements

We are grateful to V. Chalei for contributions to the early stages of this work, A. Fahrer for providing *Caph2* mutant mice, E. Freyer for assistance with FACS, the BRF facility at the Western General Hospital and BSU facilities at the Cancer Research UK Beatson Institute (C596/A17196) for animal husbandry, A. Wheeler and the ESRIC facility for super-resolution microscopy, D. van Essen and P. Eijk for performing the whole genome sequencing experiments and I. Scheinin for assistance with mouse genome sequence analysis, M. Navarro for assistance with OP9/DL1 culture, members of the Wood and Bickmore laboratories for stimulating discussions. We thank N. Gilbert and A. Fahrer for critical reading of the manuscript. A.J.W. is a Sir Henry Dale Fellow funded by the Wellcome Trust and The

Royal Society. W.A.B and A.P.J. are funded by MRC University Unit programmes. KB receives CRUK core funding, K.R.K is a Cancer Research UK Senior Fellow. K.R.K's laboratory is supported by grants from Cancer Research UK, Bloodwise and the Kay Kendall Leukaemia Fund.

Figure Legends

Figure 1: Missense mutations in *Caph2* induce thymic lymphoma

A. Schematic of the condensin II complex (Bürmann et al. 2013; Piazza et al. 2014). The box indicates the region which is expanded in panel B. **B.** (right) 3-D structure of the Smc head domain (SmcHead) and ScpA N-terminal domain ($ScpA^N$) from *B. subtilis* (PDB ID: 3ZGX)(Bürmann et al. 2013) is shown using PyMOL. The two non-contiguous sequence regions that together form the Smc ATPase head domain are colour coded in orange ($SmcHead^N$) and green ($SmcHead^C$), respectively, while the $ScpA^N$ domain fragment is shown in pink. (left) The side-chain of the I15 equivalent residue in *B. subtilis* ScpA (I22), and its interacting residues, is depicted in sphere representation. Note that residues Y44 and M48 form part of the second α-helix, which makes direct contact with the SMC coiled-coil. **C.** Kaplan-Meier plot showing survival of $Caph2^{nes/nes}$ and $P53^{-/-}$ mutant animals. The study was terminated at 15 months and surviving animals were examined for tumours during necropsy. **D.** Flow cytometry (FC) dot plots show the distribution of thymic T cell subsets according to CD4 and CD8 expression in tissue from young adult mice (±SEM, n = 5), and in representative terminal thymic lymphomas.

Figure 2: *Caph2* mutation accelerates T cell clonal outgrowth in a *P53*-dependent manner

Pie charts show the frequency of the 5 most abundant T Cell Receptor β (TCRβ) clones (grey segments) in the thymus of animals of different genotypes at 3 weeks *post partum*, relative to the remainder of clones

detected in each sample (white segment). The percentage of the top 2 clones in each sample is listed to the right of each chart. Data for *P53* single mutant animals was published previously (Dudgeon et al. 2014), and was reanalysed through the ImmunoSeq Analyser portal on the Adaptive Biotechnologies website.

Figure 3: Tumour-causing *Caph2* mutations impair mitotic progression

A. Overview of the BrdU chase experiment to assess the progression of primary $CD4^+CD8^+$ thymocytes from S phase into M phase. **B.** Line graph showing the accumulation of $BrdU^+$ cells in M phase ($pH3S10^+$) over a four hour time course, as described in panel A. Error bars show SEM of 2 biological replicates, and are representative of two independent experiments. **C**. Mitotic phase distribution of unsynchronised $H3S10P^+$ thymocytes from *wildtype* (blue) and $Caph2^{nes/nes}$ (red) OP9-DL1 co-cultures stained with anti-H3S10P, anti-α-tubulin, and DAPI. Cells staining positive for the mitotic marker H3S10P were visually assigned to one of three mitotic phase categories. Data were pooled from two biological replicate experiments (n = 59 mitotic cells for $Caph2^{+/+}$ and 111 for $Caph2^{nes/nes}$. * two-tailed Fisher's exact $p < 0.003$ **D.** Examples of anaphase/telophase cells following MG132 washout in $Caph2^{nes/nes}$ OP9/DL1 co-cultures, co-stained for α-tubulin (green), H3S10P (red) and DAPI (blue). For clarity, tubulin staining is shown only in the multipolar spindle image. Scale bars = 3μM. **E.** % normal and abnormal anaphase/telophase T cells from OP9/DL1 co-cultures 1 hour following MG132 washout for wild-type and *Caph2* mutant. Data represent one

experiment **F**. Structured Illumination Microscopy (SIM) images of DAPI-stained metaphase chromosomes from *wildtype* (top) and *Caph2*$^{nes/nes}$ (bottom) cells. Images are representative of >30 metaphase spreads from three independent experiments.

Figure 4: Mitotic perturbation arises specifically in the tumour-initiating cell population

Flow cytometry histograms show cellular DNA content profiles during differentiation of T and B lymphocytes from multipotent progenitors *in vivo*. Tissues were harvested at 6 - 8 weeks, before tumours are first detected. The tumour initiating cell population (DP CD71^{+}) is highlighted with a red box. Gates represent the 4N and >4N populations, which are quantified here for the tumour-initiating cell population and for all B and T cell subsets in Figure S5. B cells subsets were classified into Hardy Fractions A-F (Hardy et al. 1991). Gating schemes used to identify each population are shown in Figure S6, and cell surface markers and antibodies are listed in Table S5 and Table S6, respectively. Each histogram represents at least 2000 cells, and is representative of three biological replicates for progenitor subsets, and five biological replicates for T cell and B cell subsets.

Figure 5: Widespread DNA damage in *Caph2* mutant thymocytes

A. Multispectral images showing representative thymocytes from different cell cycle stages, classified based on DNA content and BrdU incoroporation. Images were acquired on an ImageStream Flow Cytometer using a 60X

objective. **B**. Histogram showing the percentage of cells with at least one bright γH2AX focus at different cell cycle stages. **C**. Histogram showing the frequency of γH2AX foci per nucleus across all cell cycle stages. For panels B & C, error bars show SEM of *n* = 3 biological replicate experiments, each comprising 10,000 cells per sample.

Figure 6: Genome doubling causes cell cycle exit in *Caph2* mutant thymocytes

A. FC contour plots, gated on $CD4^{+}CD8^{+}$ thymocytes from 6 - 12 week animals, showing a substantial increase in the proportion of abnormally large (FSC^{hi}) non-proliferating ($BrdU^{-}$) cells in $Caph2^{nes/nes}$ animals. Percentages represent mean values from three biological replicates. **B.** Contour plots presented as in panel A, with proliferation status measured by cell surface expression of CD71. Gates that define populations 1 – 4 in panel C are shown in red. Percentages represent mean values from three biological replicates. **C.** DNA content of populations 1 - 4 from panel B, determined by FC quantification of DAPI fluorescence. The non-cycling population that is greatly expanded in the $Caph2^{nes/nes}$ mutant thymus ($FSC^{hi}CD71^{lo}$) is exclusively 4N. Data are representative of five biological replicates. **D.** FISH analysis of FACS-purified non-proliferating large thymocytes (populations 2 and 4 in panel B), using a chromosome 2 (Chr2) exome paint (red), and a probe (green) corresponding to the *HoxD* locus (HoxD) on Chr2 (top). Two paired fosmid signals per nucleus are visible in population 2, whereas population 4 has four individual signals per nucleus indicating absence of sister chromatid

cohesion. Quantification of spatially separated (>0.5μM) HoxD signals is depicted in the histogram (bottom). Data are pooled from 2 biological replicates (*Caph2*$^{+/+}$ *n* = 81, *Caph2*$^{nes/nes}$ *n* = 68).

Figure 7: *P53* status determines the frequency of whole chromosome and segmental aneuploidy in *Caph2* mutant tumours

A. Example Copy Number Aberration (CNA) plots showing read depth from shallow whole genome sequencing of *Caph2*$^{nes/nes}$, P53$^{-/-}$ and *Caph2*$^{nes/nes}$ *P53*$^{-/-}$ double mutant tumours. Copy number gains are shown in red, deletions in blue. Additional plots are shown in Figure S9. **B**. Frequency of whole chromosome aneuploidies, based on shallow whole genome sequencing in tumours arising on the indicated genotypes, and control DNA from aged (9 – 15 month) *Caph2*$^{nes/nes}$ tail. Red bars indicate the mean and error bars show SEM. Brackets above the plot link conditions for which two-tailed t-tests gave significant *p* values (< 0.001) **C.** Frequency of CNAs ≥1Mb, presented as in panel B. Error bars link conditions for which two-tailed t-tests gave significant *p* values (< 0.03). **D.** Frequency of CNAs ≥30kb, presented as in panel B. Error bars link conditions for which two-tailed t-tests gave significant *p* values (< 0.05).

References

Ahmad S, Gromiha M, Fawareh H, Sarai A. 2004. ASAView: database and tool for solvent accessibility representation in proteins. *BMC Bioinformatics* **5**: 51.

Boyle S, Rodesch MJ, Halvensleben HA, Jeddeloh JA, Bickmore WA. 2011. Fluorescence in situ hybridization with high-complexity repeat-free oligonucleotide probes generated by massively parallel synthesis. *Chromosome Res* **19**: 901–909.

Brekelmans P, van Soest P, Voerman J, Platenburg PP, Leenen PJM, van Ewijk W. 1994. Transferrin Receptor Expression as a Marker of Immature Cycling Thymocytes in the Mouse. *Cellular Immunology* **159**: 331–339.

Bürmann F, Shin H-C, Basquin J, Soh Y-M, Giménez-Oya V, Kim Y-G, Oh B-H, Gruber S. 2013. An asymmetric SMC–kleisin bridge in prokaryotic condensin. *Nat Struct Mol Biol* **20**: 371–379.

Carlson CS, Emerson RO, Sherwood AM, Desmarais C, Chung M-W, Parsons JM, Steen MS, LaMadrid-Herrmannsfeldt MA, Williamson DW, Livingston RJ, et al. 2013. Using synthetic templates to design an unbiased multiplex PCR assay. *Nat Comms* **4**.

Combet C. 2000. NPS@: Network Protein Sequence Analysis. *Trends in Biochemical Sciences* **25**: 147–150.

Coschi CH, Ishak CA, Gallo D, Marshall A, Talluri S, Wang J, Cecchini MJ, Martens AL, Percy V, Welch I, et al. 2014. Haploinsufficiency of an RB-E2F1-Condensin II complex leads to aberrant replication and aneuploidy. *Cancer Discov* **4**: 840–853.

Coschi CH, Martens AL, Ritchie K, Francis SM, Chakrabarti S, Berube NG, Dick FA. 2010. Mitotic chromosome condensation mediated by the retinoblastoma protein is tumor-suppressive. *Genes & Development* **24**: 1351–1363.

Cuylen S, Metz J, Haering CH. 2011. Condensin structures chromosomal DNA through topological links. *Nat Struct Mol Biol* **18**: 894–901.

de Pooter R, Zúñiga-Pflücker JC. 2007. T-cell potential and development in vitro: the OP9-DL1 approach. *Current Opinion in Immunology* **19**: 163–168.

Derrien T, Estellé J, Marco Sola S, Knowles DG, Raineri E, Guigo R, Ribeca P. 2012. Fast computation and applications of genome mappability. ed. C.A. Ouzounis. *PLoS ONE* **7**: e30377.

Donehower LA, Harvey M, Slagle BL, McArthur MJ, Montgomery CA, Butel JS, Allan. 1992. Mice deficient for p53 are developmentally normal but

susceptible to spontaneous tumours. *, Published online: 19 March 1992;* | *doi:101038/356215a0* **356**: 215–221.

Dudgeon C, Chan C, Kang W, Sun Y, Emerson R, Robins H, Levine AJ. 2014. The evolution of thymic lymphomas in p53 knockout mice. *Genes & Development* **28**: 2613–2620.

Eskeland R, Leeb M, Grimes GR, Kress C, Boyle S, Sproul D, Gilbert N, Fan Y, Skoultchi AI, Wutz A. 2010. Ring1B Compacts Chromatin Structure and Represses Gene Expression Independent of Histone Ubiquitination. *Molecular Cell* **38**: 452–464.

Fujiwara T, Bandi M, Nitta M, Ivanova EV, Bronson RT, Pellman D. 2005. Cytokinesis failure generating tetraploids promotes tumorigenesis in p53-null cells. *Nature* **437**: 1043–1047.

Gnerre S, Maccallum I, Przybylski D, Ribeiro FJ, Burton JN, Walker BJ, Sharpe T, Hall G, Shea TP, Sykes S, et al. 2011. High-quality draft assemblies of mammalian genomes from massively parallel sequence data. *Proc Natl Acad Sci USA* **108**: 1513–1518.

Gosling KM, Makaroff LE, Theodoratos A, Kim Y-H, Whittle B, Rui L, Wu H, Hong NA, Kennedy GC, Fritz J-A, et al. 2007. A mutation in a chromosome condensin II subunit, kleisin β, specifically disrupts T cell development. *Proceedings of the National Academy of Sciences* **104**: 12445–12450.

Gouet P, Robert X, Courcelle E. 2003. ESPript/ENDscript: Extracting and rendering sequence and 3D information from atomic structures of proteins. *Nucleic Acids Research* **31**: 3320–3323.

Green LC, Kalitsis P, Chang TM, Cipetic M, Kim JH, Marshall O, Turnbull L, Whitchurch CB, Vagnarelli P, Samejima K, et al. 2012. Contrasting roles of condensin I and condensin II in mitotic chromosome formation. *Journal of Cell Science* **125**: 1591–1604.

Gruber S, Haering CH, Nasmyth K. 2003. Chromosomal Cohesin Forms a Ring. *Cell* **112**: 765–777.

Gutierrez A, Kentsis A, Sanda T, Holmfeldt L, Chen S-C, Zhang J, Protopopov A, Chin L, Dahlberg SE, Neuberg DS, et al. 2011. The BCL11B tumor suppressor is mutated across the major molecular subtypes of T-cell acute lymphoblastic leukemia. *Blood* **118**: 4169–4173.

Ham MF, Takakuwa T, Rahadiani N, Tresnasari K, Nakajima H, Aozasa K. 2007. Condensin mutations and abnormal chromosomal structures in pyothorax-associated lymphoma. *Cancer Science* **98**: 1041–1047.

Hardy RR, Carmack CE, Shinton SA, Kemp JD, Hayakawa K. 1991. Resolution and characterization of pro-B and pre-pro-B cell stages in

normal mouse bone marrow. *Journal of Experimental Medicine* **173**: 1213–1225.

Hirano T. 2012. Condensins: universal organizers of chromosomes with diverse functions. *Genes & Development* **26**: 1659–1678.

Hirota T, Gerlich D, Koch B, Ellenberg J, Peters J-M. 2004. Distinct functions of condensin I and II in mitotic chromosome assembly. *Journal of Cell Science* **117**: 6435–6445.

Houlard M, Godwin J, Metson J, Lee J, Hirano T, Nasmyth K. 2015. Condensin confers the longitudinal rigidity of chromosomes. *Nat Cell Biol* **17**: 771–781.

Jacks T, Remington L, Williams BO, Schmitt EM, Halachmi S, Bronson RT, Weinberg RA. 1994. Tumor spectrum analysis in p53-mutant mice. *Current Biology* **4**: 1–7.

Kamada K, Miyata M, Hirano T. 2013. Molecular Basis of SMC ATPase Activation: Role of Internal Structural Changes of the Regulatory Subcomplex ScpAB. *Structure* **21**: 581–594.

Kastan MB, Onyekwere O, Sidransky D, Vogelstein B, Craig RW. 1991. Participation of p53 protein in the cellular response to DNA damage. *Cancer Research* **51**: 6304–6311.

Kataoka K, Nagata Y, Kitanaka A, Shiraishi Y, Shimamura T, Yasunaga J-I, Totoki Y, Chiba K, Sato-Otsubo A, Nagae G, et al. 2015. Integrated molecular analysis of adult T cell leukemia/lymphoma. *Nat Genet* **47**: 1304–1315.

Leiserson MDM, Vandin F, Wu H-T, Dobson JR, Eldridge JV, Thomas JL, Papoutsaki A, Kim Y, Niu B, McLellan M, et al. 2014. Pan-cancer network analysis identifies combinations of rare somatic mutations across pathways and protein complexes. *Nat Genet*.

Longworth MS, Herr A, Ji JY, Dyson NJ. 2008. RBF1 promotes chromatin condensation through a conserved interaction with the Condensin II protein dCAP-D3. *Genes & Development* **22**: 1011–1024.

Losada A, Hirano T. 2005. Dynamic molecular linkers of the genome: the first decade of SMC proteins. *Genes & Development* **19**: 1269–1287.

Lowe SW, Schmitt EM, Smith SW, Osborne BA, Jacks T. 1993. p53 is required for radiation-induced apoptosis in mouse thymocytes. *, Published online: 29 April 1993; | doi:101038/362847a0* **362**: 847–849.

Manning AL, Longworth MS, Dyson NJ. 2010. Loss of pRB causes centromere dysfunction and chromosomal instability. *Genes & Development* **24**: 1364–1376.

Nasmyth K, Haering CH. 2005. THE STRUCTURE AND FUNCTION OF SMC AND KLEISIN COMPLEXES. *Annu Rev Biochem* **74**: 595–648.

Nasmyth K, Oliveira RA. 2010. Splitting the Nucleus What's Wrong with the Tripartite Ring Model? *Cold Spring Harb Symp Quant Biol* **75**: 375–388.

Nelms KA, Goodnow CC. 2001. Genome-Wide ENU Mutagenesis to Reveal Immune Regulators. *Immunity* **15**: 409–418.

Neumann B, Walter T, Hériché J-K, Bulkescher J, Erfle H, Conrad C, Rogers P, Poser I, Held M, Liebel U, et al. 2010. Phenotypic profiling of the human genome by time-lapse microscopy reveals cell division genes. *Nature* **464**: 721–727.

Nishide K, Hirano T. 2014. Overlapping and Non-overlapping Functions of Condensins I and II in Neural Stem Cell Divisions. *PLoS Genet* **10**: e1004847.

Onn I, Aono N, Hirano M, Hirano T. 2007. Reconstitution and subunit geometry of human condensin complexes. *The EMBO Journal* **26**: 1024–1034.

Ono T, Fang Y, Spector DL, Hirano T. 2004. Spatial and Temporal Regulation of Condensins I and II in Mitotic Chromosome Assembly in Human Cells. *Mol Biol Cell* **15**: 3296–3308.

Ono T, Losada A, Hirano M, Myers MP, Neuwald AF, Hirano T. 2003. Differential Contributions of Condensin I and Condensin II to Mitotic Chromosome Architecture in Vertebrate Cells. *Cell* **115**: 109–121.

Parris CN, Adam Zahir S, Al-Ali H, Bourton EC, Plowman C, Plowman PN. 2015. Enhanced γ-H2AX DNA damage foci detection using multimagnification and extended depth of field in imaging flow cytometry. *Cytometry A* **87**: 717–723.

Piazza I, Rutkowska A, Ori A, Walczak M, Metz J, Pelechano V, Beck M, Haering CH. 2014. Association of condensin with chromosomes depends on DNA binding by its HEAT-repeat subunits. *Nat Struct Mol Biol* **21**: 560–568.

Rawlings JS, Gatzka M, Thomas PG, Ihle JN. 2010. Chromatin condensation via the condensin II complex is required for peripheral T-cell quiescence. *The EMBO Journal* **30**: 263–276.

Scheinin I, Sie D, Bengtsson H, van de Wiel MA, Olshen AB, van Thuijl HF, van Essen HF, Eijk PP, Rustenburg F, Meijer GA, et al. 2014. DNA copy number analysis of fresh and formalin-fixed specimens by shallow whole-genome sequencing with identification and exclusion of problematic regions in the genome assembly. *Genome Research* **24**: 2022–2032.

Sheltzer JM, Torres EM, Dunham MJ, Amon A. 2012. Transcriptional consequences of aneuploidy. *Proceedings of the National Academy of Sciences* **109**: 12644–12649.

Shintomi K, Hirano T. 2011. The relative ratio of condensin I to II determines chromosome shapes. *Genes & Development* **25**: 1464–1469.

Smith ED, Xu Y, Tomson BN, Leung CG, Fujiwara Y, Orkin SH, Crispino JD. 2004. More than blood, a Novel Gene Required for Mammalian Postimplantation Development. *Molecular and Cellular Biology* **24**: 1168–1173.

Söding J, Biegert A, Lupas AN. 2005. The HHpred interactive server for protein homology detection and structure prediction. *Nucleic Acids Research*.

Swedlow JR, Hirano T. 2003. The Making of the Mitotic Chromosome: Modern Insights into Classical Questions. *Molecular Cell* **11**: 557–569.

Thompson SL, Compton DA. 2010. Proliferation of aneuploid human cells is limited by a p53-dependent mechanism. *The Journal of Cell Biology* **188**: 369–381.

Tina KG, Bhadra R, Srinivasan N. 2007. PIC: Protein Interactions Calculator. *Nucleic Acids Research* **35**: W473–W476.

Torres EM, Sokolsky T, Tucker CM, Chan LY, Boselli M, Dunham MJ, Amon A. 2007. Effects of Aneuploidy on Cellular Physiology and Cell Division in Haploid Yeast. *Science* **317**: 916–924.

van Thuijl HF, Scheinin I, Sie D, Alentorn A, van Essen HF, Cordes M, Fleischeuer R, Gijtenbeek AM, Beute G, van den Brink WA, et al. 2014. Spatial and temporal evolution of distal 10q deletion, a prognostically unfavorable event in diffuse low-grade gliomas. *Genome Biol* **15**: 471.

Venkatraman ES, Olshen AB. 2007. A faster circular binary segmentation algorithm for the analysis of array CGH data. *Bioinformatics* **23**: 657–663.

Williams BR, Prabhu VR, Hunter KE, Glazier CM, Whittaker CA, Housman DE, Amon A. 2008. Aneuploidy Affects Proliferation and Spontaneous Immortalization in Mammalian Cells. *Science* **322**: 703–709.

Wood AJ, Severson AF, Meyer BJ. 2010. Condensin and cohesin complexity: the expanding repertoire of functions. *Nat Rev Genet* **11**: 391–404.

Zhang J, Ding L, Holmfeldt L, Wu G, Heatley SL, Payne-Turner D, Easton J, Chen X, Wang J, Rusch M, et al. 2012. The genetic basis of early T-cell precursor acute lymphoblastic leukaemia. *Nature* **481**: 157–163.

A

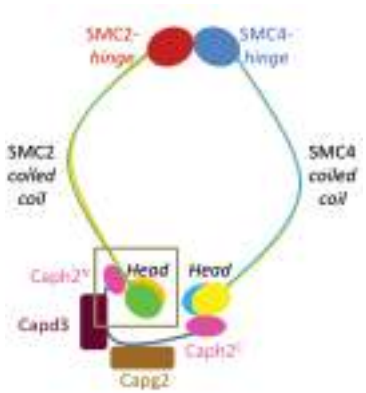
SMC2-hinge
SMC4-hinge
SMC2 coiled coil
SMC4 coiled coil
Caph2
Head
Head
Capd3
Caph2
Capg2

B

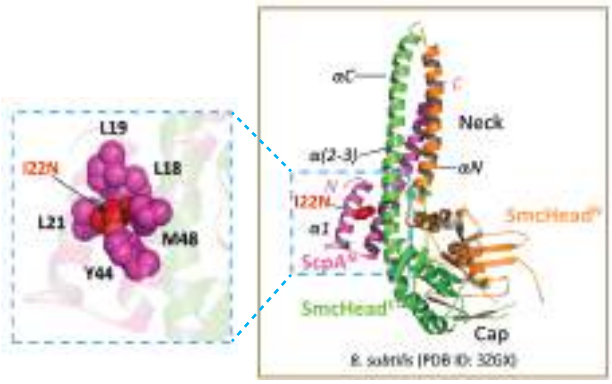
L19
I22N
L18
L21
M48
Y44
αC
Neck
α(2-3)
αN
I22N
α1
ScpA
SmcHead
Cap

C

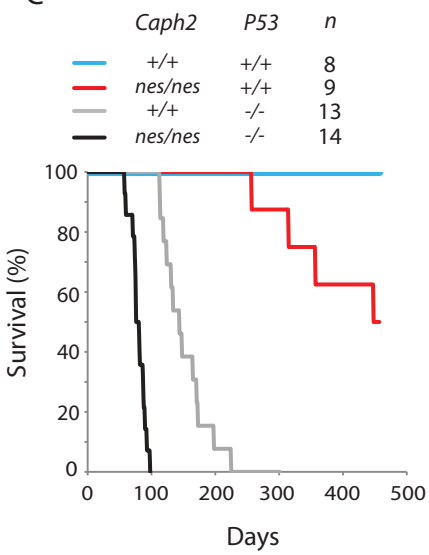
Caph2 P53 n
+/+ +/+ 8
nes/nes +/+ 9
+/+ -/- 13
nes/nes -/- 14
Survival (%)
Days
0
20
40
60
80
100
0
100
200
300
400
500

D

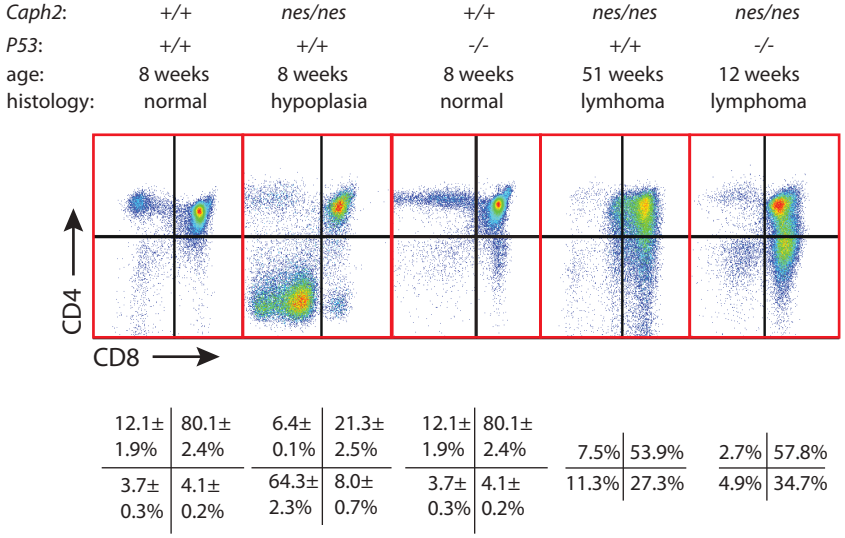
Caph2: +/+ nes/nes +/+ nes/nes nes/nes
P53: +/+ +/+ -/- +/+ -/-
age: 8 weeks 8 weeks 8 weeks 51 weeks 12 weeks
histology: normal hypoplasia normal lymhoma lymphoma
CD4
CD8
12.1± 1.9% 80.1± 2.4%
3.7± 0.3% 4.1± 0.2%
6.4± 0.1% 21.3± 2.5%
64.3± 2.3% 8.0± 0.7%
12.1± 1.9% 80.1± 2.4%
3.7± 0.3% 4.1± 0.2%
7.5% 53.9%
11.3% 27.3%
2.7% 57.8%
4.9% 34.7%

A

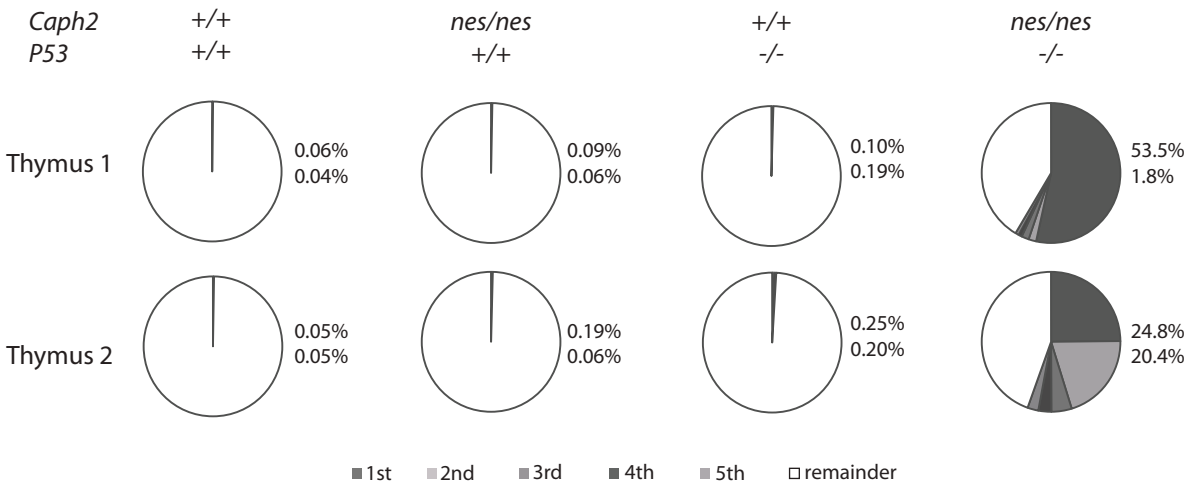
Caph2
P53
+/+
+/+
nes/nes
+/+
+/+
-/-
nes/nes
-/-
Thymus 1
0.06%
0.04%
0.09%
0.06%
0.10%
0.19%
53.5%
1.8%
Thymus 2
0.05%
0.05%
0.19%
0.06%
0.25%
0.20%
24.8%
20.4%
1st
2nd
3rd
4th
5th
remainder

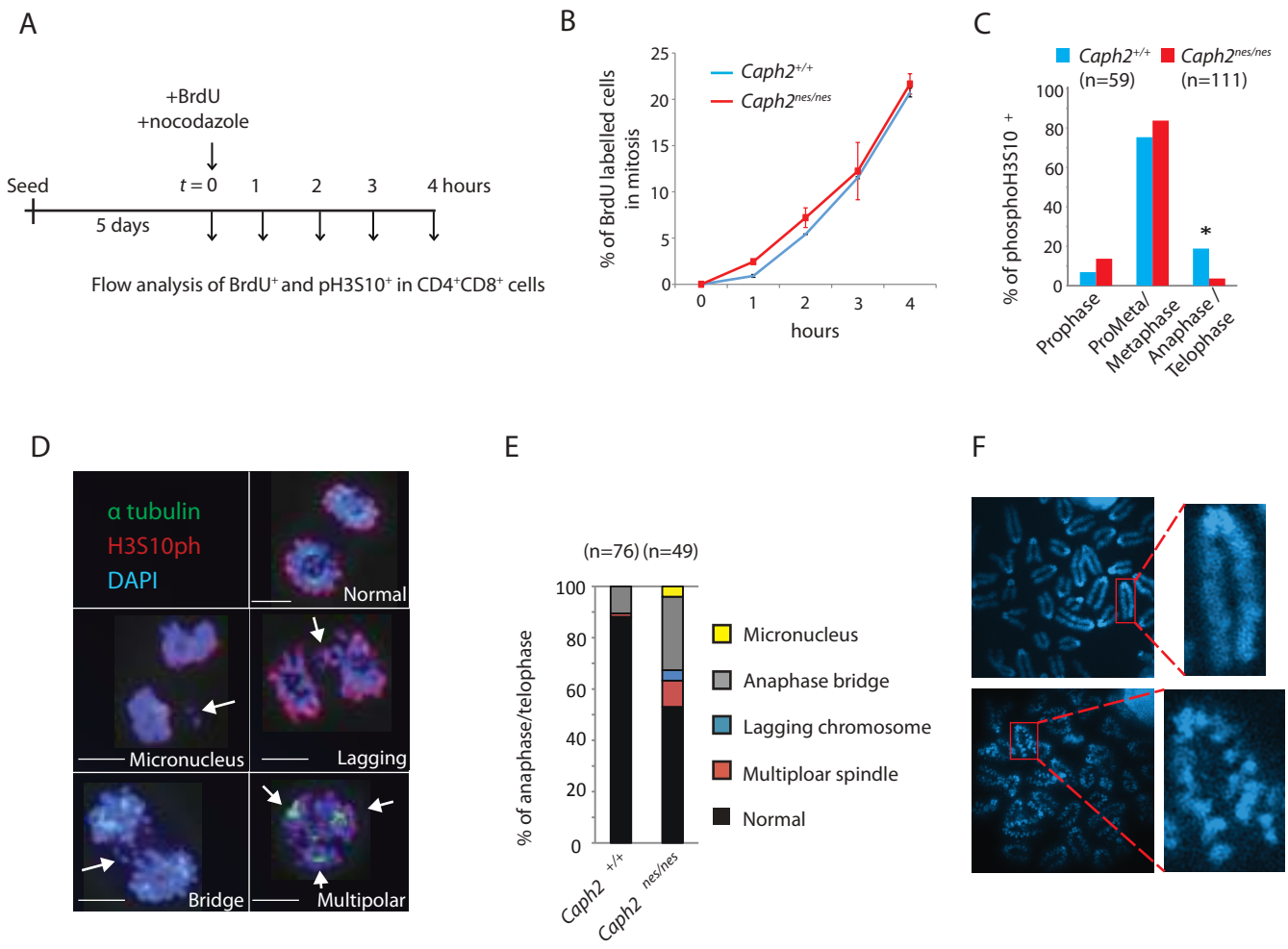
A
+BrdU
+nocodazole
Seed
t = 0
1
2
3
4 hours
5 days
Flow analysis of BrdU+ and pH3S10+ in CD4+CD8+ cells
B
% of BrdU labelled cells in mitosis
Caph2+/+
Caph2nes/nes
hours
C
Caph2+/+ (n=59)
Caph2nes/nes (n=111)
% of phosphoH3S10 +
Prophase
ProMeta/ Metaphase
Anaphase / Telophase
D
α tubulin
H3S10ph
DAPI
Normal
Micronucleus
Lagging
Bridge
Multipolar
E
(n=76) (n=49)
% of anaphase/telophase
Micronucleus
Anaphase bridge
Lagging chromosome
Multiploar spindle
Normal
Caph2 +/+
Caph2 nes/nes
F

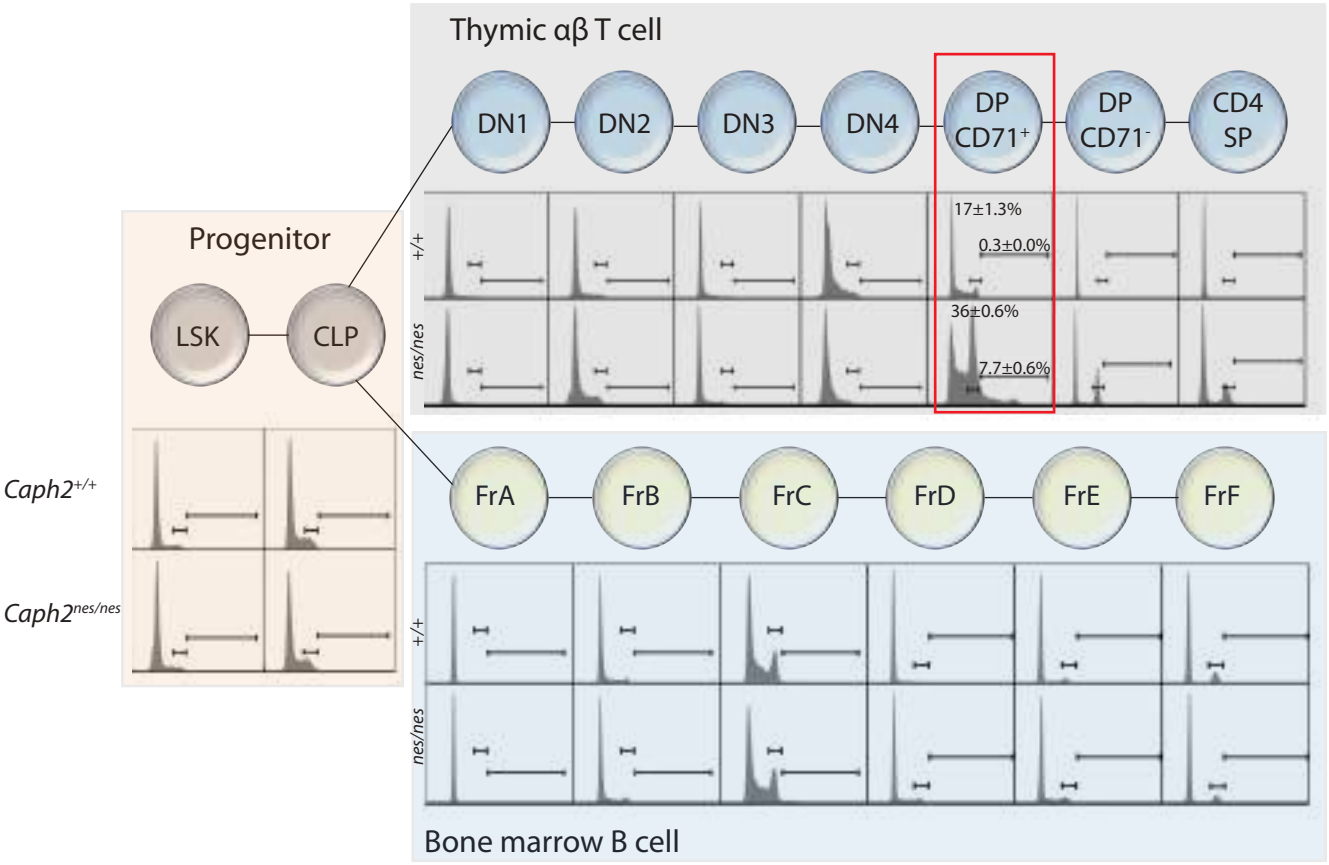
Thymic αβ T cell
DN1
DN2
DN3
DN4
DP CD71+
DP CD71-
CD4 SP
17±1.3%
0.3±0.0%
36±0.6%
7.7±0.6%
+/+
nes/nes
Progenitor
LSK
CLP
Caph2+/+
Caph2nes/nes
FrA
FrB
FrC
FrD
FrE
FrF
+/+
nes/nes
Bone marrow B cell

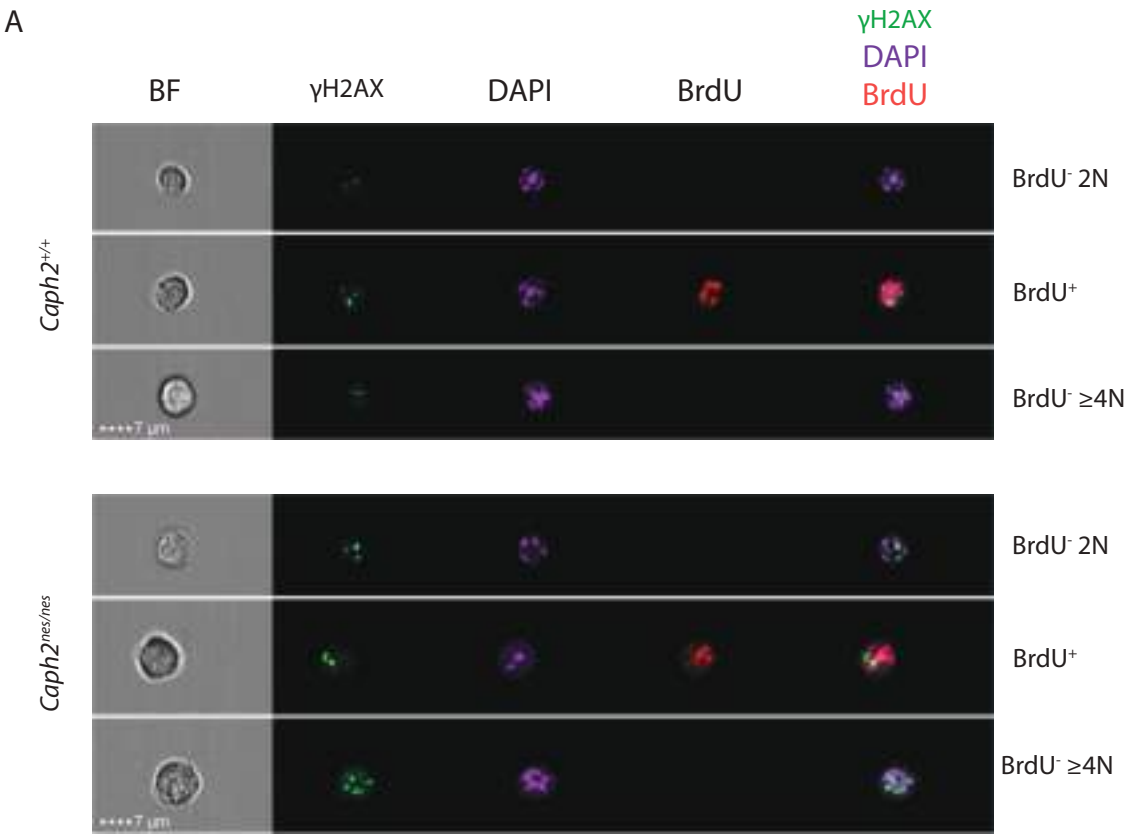
A
γH2AX
DAPI
BrdU
BF
γH2AX
DAPI
BrdU
Caph2+/+
Caph2nes/nes
BrdU- 2N
BrdU+
BrdU- ≥4N
BrdU- 2N
BrdU+
BrdU- ≥4N

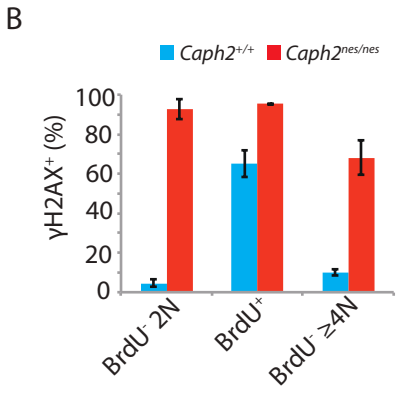
B
Caph2+/+
Caph2nes/nes
γH2AX+ (%)
100
80
60
40
20
0
BrdU- 2N
BrdU+
BrdU- ≥4N

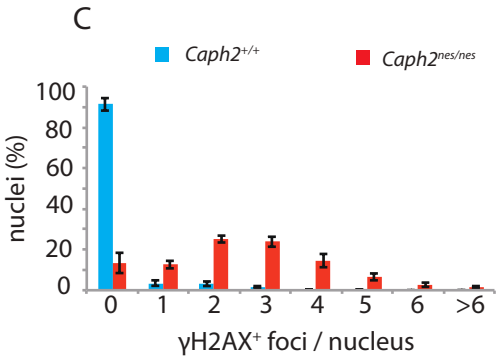
C
Caph2+/+
Caph2nes/nes
nuclei (%)
100
80
60
40
20
0
0
1
2
3
4
5
6
>6
γH2AX+ foci / nucleus

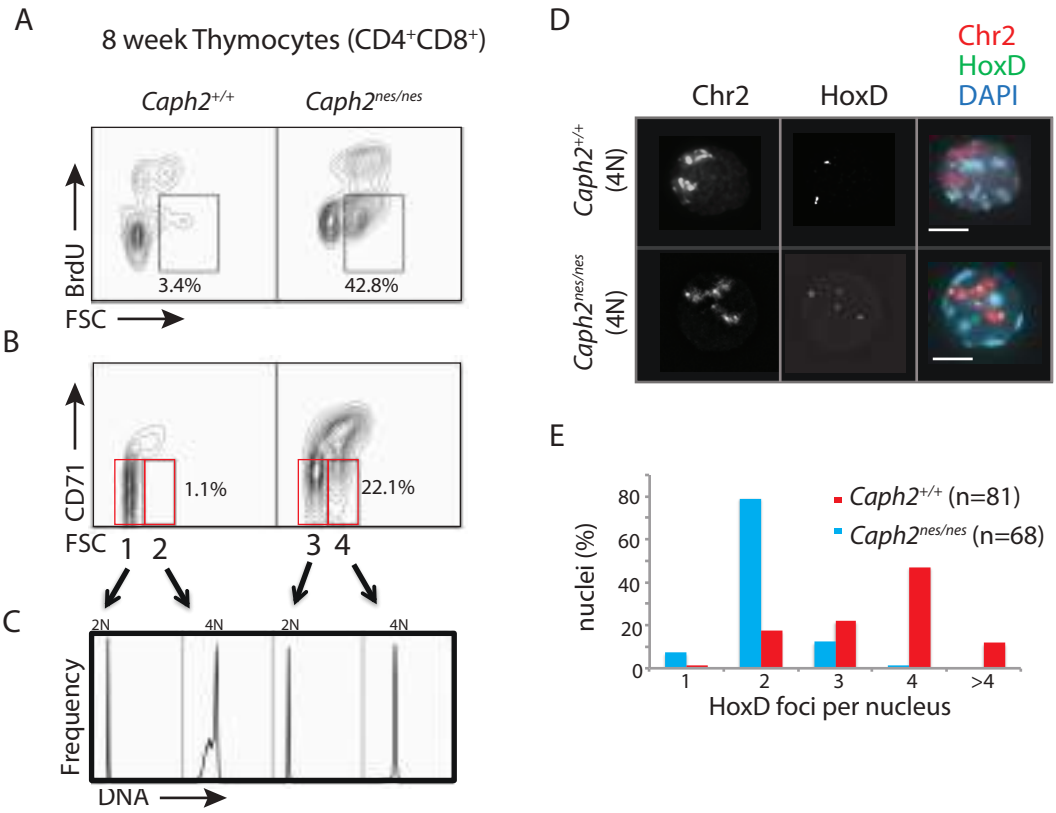
A
8 week Thymocytes (CD4+CD8+)
Caph2+/+
Caph2nes/nes
BrdU
FSC
3.4%
42.8%
B
CD71
FSC
1.1%
22.1%
1 2
3 4
C
2N
4N
2N
4N
Frequency
DNA
D
Chr2
HoxD
DAPI
Chr2
HoxD
Caph2+/+ (4N)
Caph2nes/nes (4N)
E
nuclei (%)
80
60
40
20
0
Caph2+/+ (n=81)
Caph2nes/nes (n=68)
1
2
3
4
>4
HoxD foci per nucleus

A

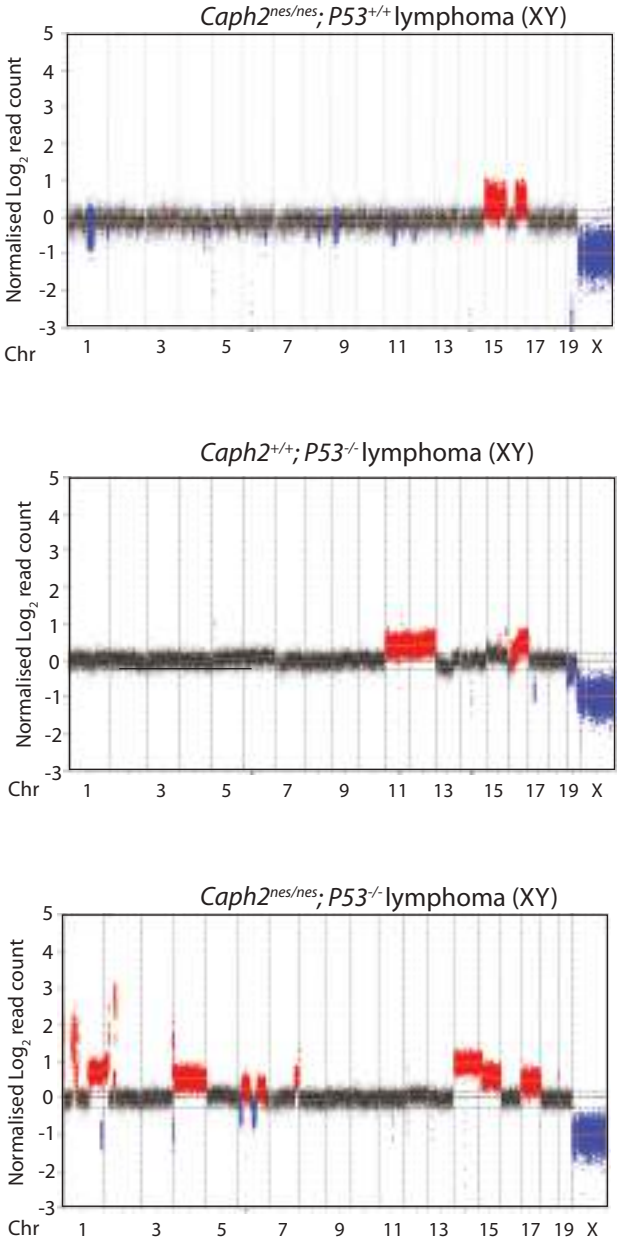
Caph2nes/nes; P53+/+ lymphoma (XY)
Caph2+/+; P53-/- lymphoma (XY)
Caph2nes/nes; P53-/- lymphoma (XY)
Normalised Log2 read count
Chr
1 3 5 7 9 11 13 15 17 19 X

B

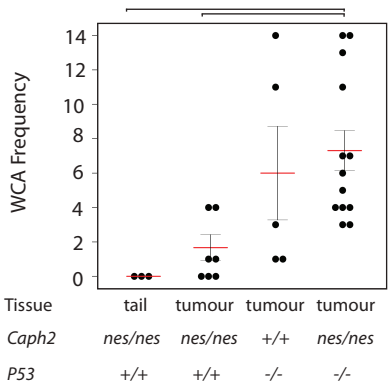
WCA Frequency
Tissue tail tumour tumour tumour
Caph2 nes/nes nes/nes +/+ nes/nes
P53 +/+ +/+ -/- -/-

C

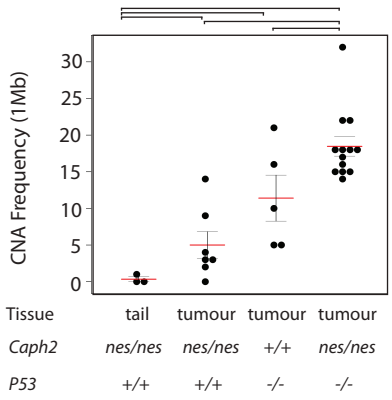
CNA Frequency (1Mb)
Tissue tail tumour tumour tumour
Caph2 nes/nes nes/nes +/+ nes/nes
P53 +/+ +/+ -/- -/-

D

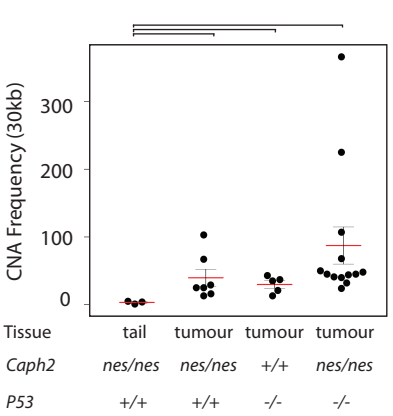
CNA Frequency (30kb)
Tissue tail tumour tumour tumour
Caph2 nes/nes nes/nes +/+ nes/nes
P53 +/+ +/+ -/- -/-